RESEARCH PAPER

Dynamic tensile and failure behavior of bi-directional reinforced GFRP materials

Zishang Liu[1,2] · Zhe Yang[2] · Yuchao Chen[1,2] · Yangyang Yu[3] · Yanpeng Wei[1,2] · Maohui Li[4] · Chenguang Huang[2]

Abstract

In this paper, a series of static/dynamic tensile tests are performed for glass fiber reinforced plastic (GFRP) composites. Using the combination of high-speed photography and digital image correlation (DIC) technology, true stress–strain curves in different directions and strain rates are obtained. We also obtained the dynamic failure strain of the material in different directions, which are used to accurately describe the dynamic tensile and failure behavior of the material. The experimental results show that there is a stiffness change point N in three directions under different strain rate (10^{-3} s^{-1}, 10 s^{-1}, 100 s^{-1}) tensile conditions. The stiffness before and after N point is recorded as $E_{initial}$ and $E_{changed}$ respectively. The values of $E_{changed}$ in weft direction and warp direction are about 30% to 50% of $E_{initial}$, while $E_{changed}$ in tilt direction is only about 10% of $E_{initial}$. The fiber has the highest strength in the weft direction and the tilt direction has the lowest strength. With the combination of high-speed photography and DIC technology, the dynamic failure parameters of different directions under the strain rate of 100 s^{-1} are obtained. The dynamic failure strains in three directions are 0.245, 0.373 and 0.341, respectively. The parameters are verified by impact three-point bending test. These works can more accurately describe the dynamic mechanical behavior of glass fiber reinforced plastic (GFRP) composites and provide reference for the design of GFRP structures.

Keywords Solid mechanics · Dynamic failure strain · Digital image correlation · Strain rate effect · Stiffness

1 Introduction

Glass fiber reinforced plastic (GFRP) is a typical composite material which has many uses in industry and life. GFRP has many advantages, such as heat insulation, fatigue resistance, flame retardancy, corrosion resistance, light weight, good strength, and strong designability [1–7]. Lightening of vehicle body is an important trend in the design of high-speed train [8, 9]. The lightening of the car body can reduce the consumption of resources and improve the speed of the train [10, 11]. Because of its excellent

performance, people have applied GFRP to train structures and non-structural parts [12, 13]. Because of the nonuniformity of GFRP structure, the mechanical properties are characterized by anisotropy and low interlaminar shear modulus [14, 15].

Scholars have done a lot of work in the field of mechanical behavior of GFRP composites. Shang et al. [16] obtained the dynamic constitutive equation of GFRP by Lagrange experiment. The dynamic constitutive equations were deduced from the experimental data which was obtained by Lagrange analysis. Huang et al. [17] studied the effect of strain rate and temperature on the dynamic tensile properties of unidirectional glass fiber reinforced polyester. They used the experimental results to establish a bi-modal Weibull statistical constitutive equation to describe the material. Asprone et al. [18] carried out the strain-rate controlled tensile failure tests on glass fiber-reinforced polymer specimens. The results are implemented into a constitutive model to simulate the exhibited mechanical behavior. Reis et al. [19] studied the effect of the extreme conditions on the tensile impact strength of GFRP composites. Composite laminates were immersed into solutions with different temperatures. It was

✉ Yanpeng Wei
weiyanpeng@imech.ac.cn

1 Institute of Mechanics, Chinese Academy of Sciences, Beijing 100190, China

2 University of Chinese Academy of Sciences, Beijing 100049, China

3 CRRC Qingdao Sifang Co., LTD, Qingdao 266111, China

4 The Quartermaster Research Institute of Engineering and Technology, Beijing 100010, China

observed that the impact response is substantially affected by the temperature for the same exposure time.

Digital image correlation (DIC) technology is a method to obtain deformation information of object surface by tracking the movement of geometric points on digital speckle image in different states of object surface [20–23]. The displacement field of the experimental specimens can be easily obtained by DIC method [24–27]. This method has been widely used in the field of experimental mechanics [28–33]. However, little research has been done on the analysis of strain field, accurate engineering failure strain and dynamic failure strain of bi-directional reinforced GFRP under static/dynamic tension by DIC method. There are also some shortcomings in further numerical fitting by using the obtained precise parameters.

In this paper, static/dynamic tensile tests of bi-directional reinforced GFRP composites with different directions and strain rates were carried out. By using a set of static/dynamic experimental equipment and high-speed photography combined with DIC technology, the strain information of the material in the whole field during tension was obtained, and the stress time-domain signal of the material was obtained by force sensor. The static/dynamic stress–strain curves of materials with different directions and strain rates are obtained by combining the time-domain signal results of stress and strain. The dynamic failure strains of materials with different directions and strain rates are obtained according to the results of DIC technology. The model parameters of the material are fitted by the data obtained, and the accuracy of the parameters is verified by numerical simulation and experimental results. The dynamic failure behavior of bi-directional reinforced GFRP composites is accurately described through a set of experiments and verification methods in this paper.

2 Experimental method

2.1 Experimental equipment

In this experiment, three kinds of tensile tests under different strain rates were carried out for GFRP materials, which were quasi-static (10^{-3} s^{-1}), 10 s^{-1} and 100 s^{-1}. The quasi-static (10^{-3} s^{-1}) tensile test was carried out by universal testing machine, and the other two dynamic tensile tests were carried out by intermediate-high strain rate material testing machine which was shown in Fig. 1.

Intermediate-high strain rate material testing machine can carry out material tensile test under 1–500 s^{-1} strain rate range. The core power system of the equipment is a hydraulic power system. The power output during the whole test process is provided by the hydraulic system. Tests at different strain rates can be carried out by changing the size

Fig. 1 Intermediate-high strain rate material testing machine

of test specimens. Shear or compression tests can also be carried out by changing the tooling design of materials. The machine is also equipped with a super dynamic strain gauge, so that the stress information with time can be obtained with high precision, high response and high sampling rate.

Many dynamic tension experiments were carried out by Hopkinson bar. The Hopkinson bar can be used to obtain the stress–strain curves of samples under dynamic impact conditions. The strain rate range of Hopkinson bar test is generally 10^2–10^4 s^{-1}. However, it is generally difficult for Hopkinson bar to carry out dynamic tests with strain rate below 10^2, and the traditional material testing machine is mainly used to carry out quasi-static test. From the point of view of strain rate, there is a missing test range between them. Based on this situation, the dynamic mechanical properties of materials can be studied by using intermediate-high strain rate material testing machine and Hopkinson bar, which can cover the test range of strain rate better. In the past, most of the experiments were carried out through Hopkinson bars. It is difficult to carry out the test in the middle strain rate range by using Hopkinson bar. In order to better study the mechanical properties of materials under the medium strain rate, it is necessary to use the intermediate-high strain rate material testing machine to carry out the experiment under middle strain rate.

As shown in Fig. 2, we designed a special force sensor for the tensile specimen. The force sensor designed can not only measure the force, but also prevent the specimen from sliding out in the process of tensile.

In order to get the strain field information by using DIC technology, a high-speed camera is equipped to photograph the test process. The model of the high-speed camera is Photron SA1.1. With a resolution of 1024×1024 pixels, the sampling rate can reach 5400 fps. By reducing the resolution, the sampling rate can reach up to 675,000 fps. The sampling rate of 80,000 fps is selected and the resolution is 896×120 pixels in our research. It not only can accurately

Fig. 2 Fixture for dynamic tensile test specimen

Fig. 4 Layer direction of fiber and the cutting direction of specimen

record the speckle deformation pictures of each specimen at different times, but also ensures the processing accuracy of the post-processing software. The complete set of high-speed photography equipment is shown in Fig. 3.

2.2 Preparation of samples

The test material is supplied by Qingdao Haitie Yuanxin Industrial Equipment Co., Ltd. The reinforced direction of GFRP used in the experiment is bidirectional enhancement, and the thickness of tensile test specimen is 2 mm. The cutting direction is 0°, 45° and 90°, as shown in Fig. 4. The 0° direction is marked as weft direction. The 45° direction is marked as tilt direction, and the 90° direction is marked as warp direction. It should be noted that the number of reinforcements in the two (0° and 90°) directions shown in Fig. 4 were different. Based on the application environment, the ratio of the number of reinforcements in the two (0° and 90°) directions is not 1:1.
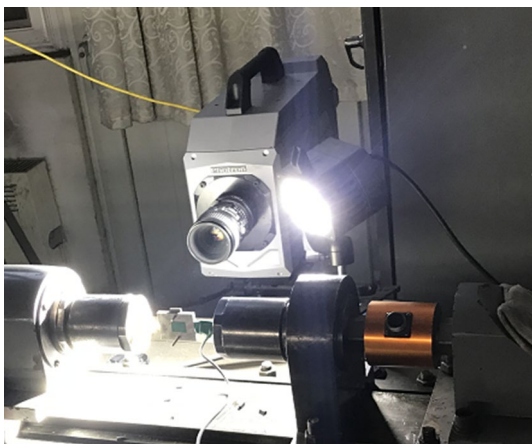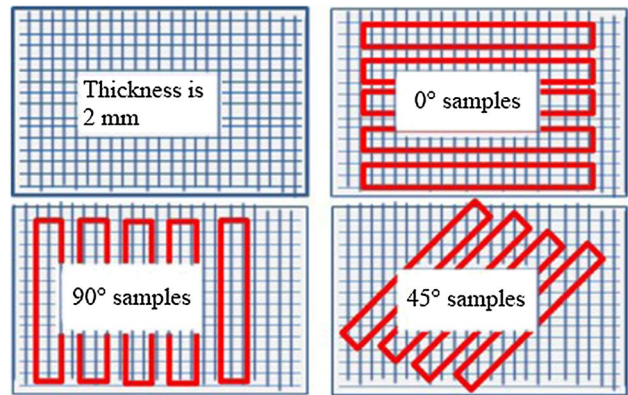
According to the different loading characteristics of quasi-static (10^{-3} s^{-1}) and dynamic tensile tests, two kinds of tensile specimens with different sizes were designed. The quasi-static (10^{-3} s^{-1}) tensile test piece size is shown in Fig. 5a, and the thickness of the specimen is 2 mm. The size of the dynamic tensile specimen is shown in Fig. 5b, and the thickness of the specimen is 2 mm. Artificial speckles were sprayed in the middle of tensile specimens to measure the deformation of GFRP specimens in the whole field.

2.3 Collection of results

The speckle is sprayed on the surface of the specimen, and the tensile process is shown in Fig. 6. High-speed photography was used to photograph the surface morphology of speckles in order to obtain the morphological changes of speckles during the whole dynamic tensile process. The time–space distribution of the displacement in the gauge section of the specimen is obtained by processing the photographs taken by high-speed photography with DIC technology, and the time–space distribution of the strain is obtained by processing the displacement–time curve. The load-time curve of the specimen during tension is obtained by force sensor, and the stress-time curve is obtained by processing the load-time curve. The stress–strain curves and dynamic failure strains of the specimens are obtained by combining the stress-time curves and the time–space distribution of the strain.

3 Experimental results and analysis

3.1 Experimental repeatability

Three repeated tests were carried out for each working condition of specific direction and strain rate, and the dispersion of the three groups of original stress–strain curves was
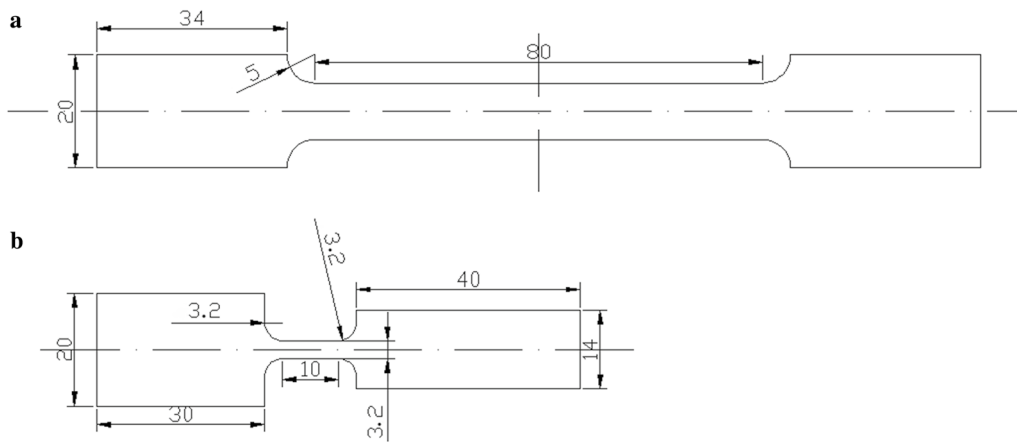

Fig. 3 High speed photographic equipment

Fig. 5 Size of experimental specimens (unit:mm)

Fig. 6 Quasi-static tensile test
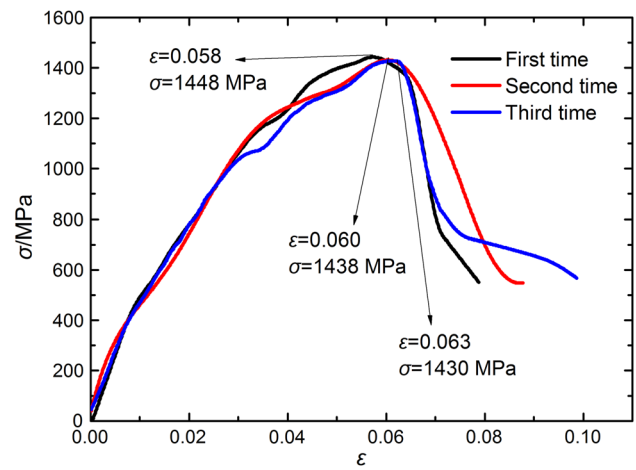

Fig. 7 Stress–strain curves of repeated tests under $100\ \mathrm{s}^{-1}$ strain rate

analyzed. The stress–strain curve, which is closer to the average value, is chosen as the representative to study the mechanical properties of materials.

The dispersion of $100\ \mathrm{s}^{-1}$ strain rate in weft direction is discussed. The stress–strain curves and failure diagrams obtained from three repeated tests are shown in Figs. 7 and 8, respectively.

Under three repeated tests, the final fracture position of the specimens occurs in the standard interval, which belongs to the effective experiment. For the discussion of data dispersion, two reference indexes are selected: engineering failure strain and strength. The analysis method is to compare the three results of the index item with the average value. After comparison, the deviations of the three indicators are 5% and 1%, respectively. In the subsequent analysis, the stress–strain curves under each working condition are compared similarly, and the maximum deviation under all working conditions is controlled in the range of 5%. The selection principle of stress–strain curve under each working condition is to select the curve with the middle value of each reference index.
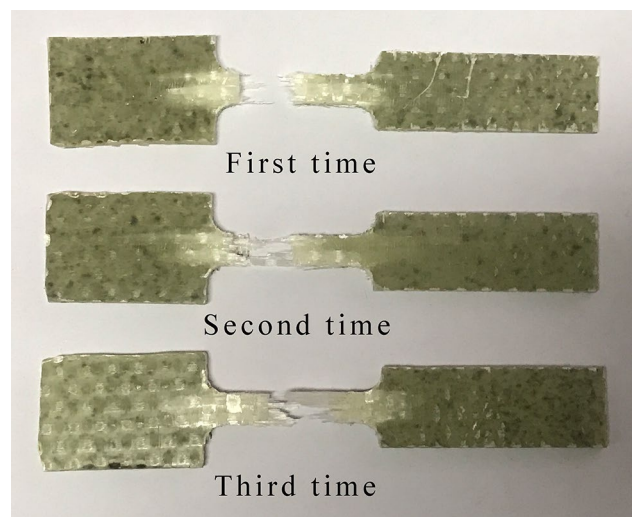

Fig. 8 Morphology of fractured specimens

3.2 Strain field under typical working conditions

The strain field in dynamic tension process was analyzed by DIC technique under the condition of strain rate of 100 s^{-1} in the weft direction. According to the analysis of strain field during the whole tensile process, the morphology and strain field of the gauge section of GFRP specimens at different time were obtained. The results are shown in Figs. 9 and 10.

Through the stress field diagram of the whole tensile process, it can be found that the strain field distribution on the surface of the material is not uniform in the initial stage of tension (Fig. 10a, b). In the mid-tensile stage (Fig. 10b, c), the non-uniformity of strain field in the material gauge section is further enhanced. By observing the real-time photographs of the tension process of the standard spacing section, it was found that the color of some areas of the standard spacing section of the specimens changed obviously in the early stage of fracture (Fig. 9d, e). Figure 10e also shows that the local strain of the specimen increases significantly. The whitening area in the photo corresponds to the significantly enlarged area in the strain field, which is the fracture failure area of the specimen. After fracture failure (Fig. 10e,
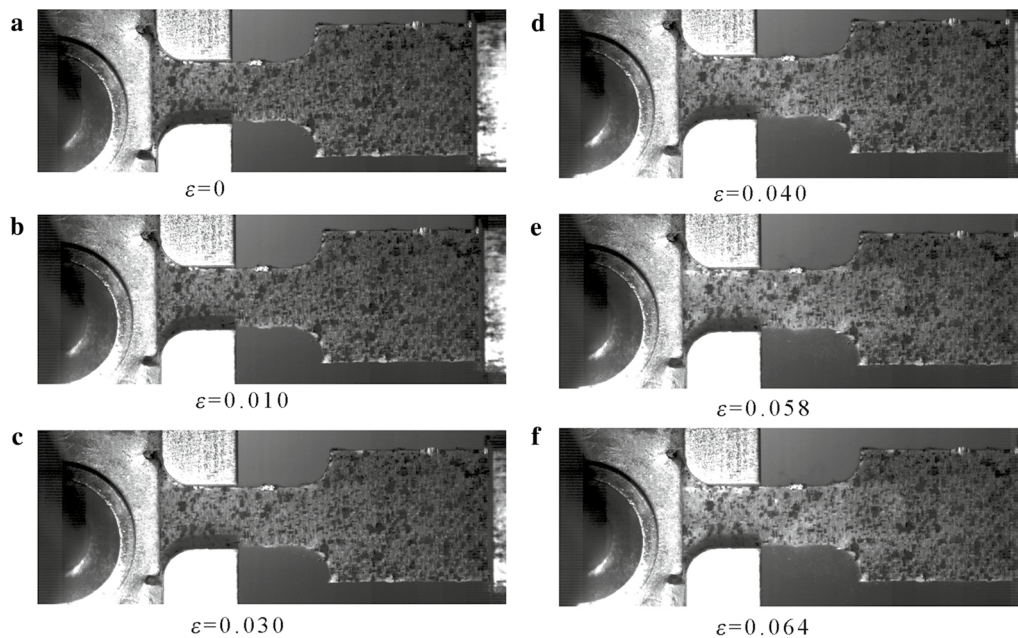

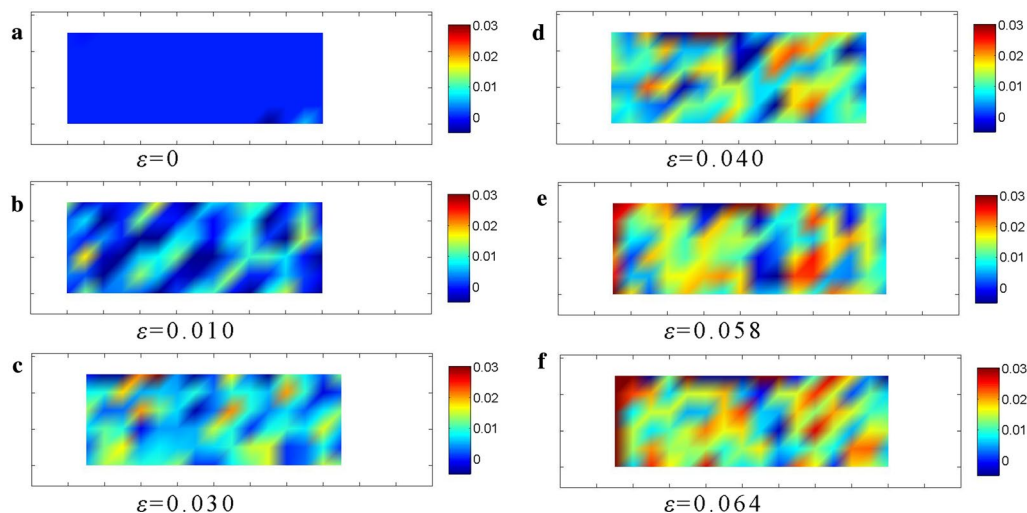**Fig. 9** Specimen morphology under 100 s^{-1} strain rate

Fig. 10 Strain field in weft direction under 100 s^{-1} strain rate

f), the specimens are destroyed. During the whole fracture process, the strain field in the tensile direction is non-uniform. In order to simulate the failure behavior of materials more accurately, it is necessary to use the stress field to analyze the local actual damage part of the gauge section.

3.3 Tensile curve of typical working condition

The stress–strain curve obtained under tension with strain rate of 100 s^{-1} in the weft direction is shown in Fig. 11. The ordinal marks in the curve are the same as those in Figs. 9 and 10.

Observing the whole dynamic tension stress–strain curve, the linearity of the curve is better in the early stages of loading. With the increase of loading stress, the stress–strain relationship gradually transits from linear to non-linear. The stiffness of the material decreases during the later stage of tension. At the end of the whole loading period, the curve drops rapidly and the specimen is suddenly destroyed. Considering the whole tensile process, the material presents non-linear and brittle failure.

Under quasi-static (10^{-3} s^{-1}) tension, the stress–strain curves of materials in the directions of weft, tilt and warp are shown in Fig. 12.

Under quasi-static (10^{-3} s^{-1}) tension, the stress–strain curve of the material is shown in Fig. 12. The strength of the three directions is 569 MPa, 158 MPa and 383 MPa respectively. The failure strain of the material is 0.028, 0.115 and 0.045. The curve in the figure is the closest to the average result of repetitive experiment. In the elastic stage, the elastic modulus E_{initial} in three directions is 30.5 GPa, 6.8 GPa and 9.9 GPa, respectively. The strength in weft direction is the largest and the engineering failure strain is the smallest. The tilt direction has the best plasticity but the smallest
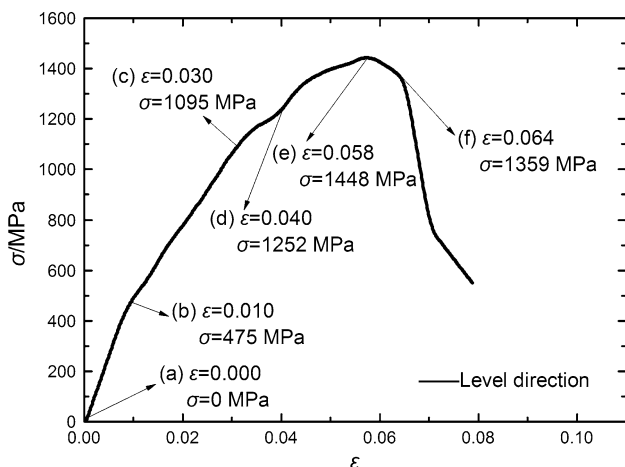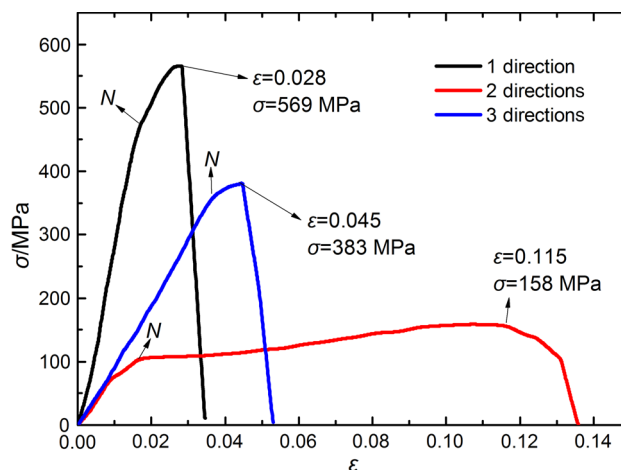

Fig. 12 Stress–strain curves in different directions under quasi-static condition

strength. The reinforcing direction of internal glass fibers is mainly in the weft and warp directions. Because the number of fiberglass bundles in weft direction is more, the strength in weft direction is 49% higher than that in warp direction. The engineering failure strain in weft direction is 76% lower than that in tilt direction. Similar to the stress–strain curve under typical working conditions in Fig. 11. The whole stretching process presents non-linear characteristics.

By observing the three curves synthetically, the original stress–strain curve can be approximately described by a bilinear constitutive model. Therefore, a corresponding stiffness change point N can be found on the curve. The stiffness of the bilinear constitutive model at different stages is expressed by the slope of the stress–strain curve before and after point N. The selection of point N is based on the following two principles: (1) choosing a clear and identifiable turning point; (2) choosing the point where the absolute value of the second derivative of the function fitted by the curve before failure takes the maximum value.

The final selected point N is shown in Fig. 12, which divides the whole tension process into two stages. The stiffness of the second stage is weaker than that of the first stage. The three directions of E_{initial} are 30.5 GPa, 6.8 GPa and 9.9 GPa, and E_{changed} are 8.8 GPa, 0.7 GPa and 2.7 GPa, respectively. The changed E_{changed} values are reduced to 28.9%, 10.3% and 27.3% of the original E_{initial} values.

The stress–strain curves of materials in different directions under three different strain rates are shown in Figs. 13, 14 and 15.

Figure 13 shows the tensile stress–strain curves at quasi-static (10^{-3} s^{-1}), 10 s^{-1} and 100 s^{-1} strain rates in weft direction. Under the three strain rates, the strength of the material is 569 MPa, 1209 MPa and 1448 MPa, respectively. The engineering failure strain is 0.028, 0.058 and 0.058. With
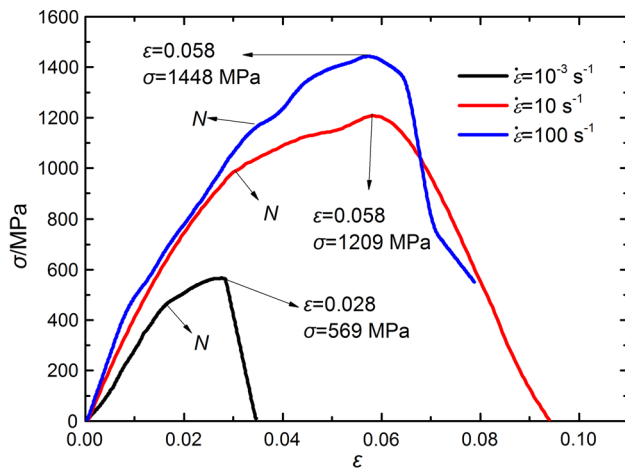

Fig. 11 Stress–strain curve of the weft direction under 100 s^{-1} strain rate

Fig. 13 Tensile stress–strain curves of the weft direction under different strain rates
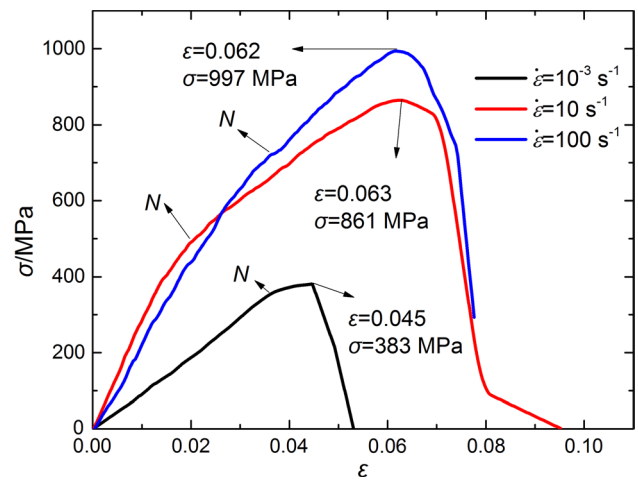

Fig. 15 Tensile stress–strain curves of the warp direction under different strain rates
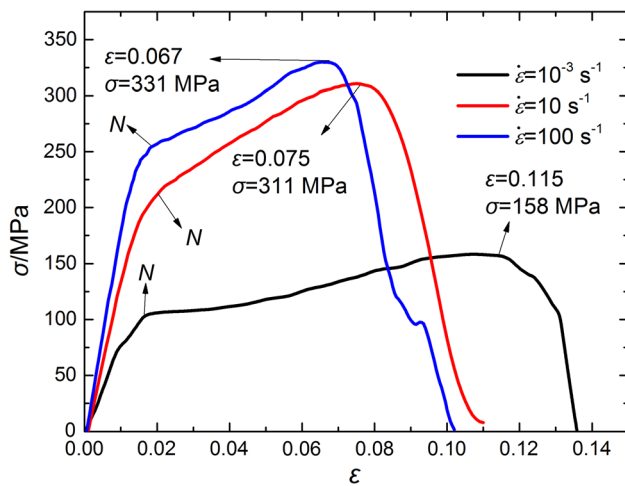

Fig. 14 Tensile stress–strain curves of the tilt direction under different strain rates

the increase of strain rate, the strength of the material is significantly enhanced. The engineering failure strain under two dynamic tension conditions is larger than that under quasi-static tension (10^{-3} s^{-1}). However, the engineering failure strain at the strain rate of 10 s^{-1} is equal to that at the strain rate of 100 s^{-1}. The engineering failure strain does not show the characteristics of increasing continuously with the increase of strain rate.

It should be pointed out that the stiffness change point is not easy to find when the strain rate is 100 s^{-1}. So we use the second derivative method to determine point N. After analysis, the absolute value of the second derivative reaches the maximum when the strain is 0.043. So the point where the strain is 0.043 is the point where the stiffness changes. Under quasi-static (10^{-3} s^{-1}) strain rate tension, the $E_{initial}$

of 30.5 GPa decreases to the $E_{changed}$ of 8.8 GPa. The strain rate of 10 s^{-1} decreases from 33.3 to 10.4 GPa, and from 28.6 to 8.4 GPa at 100 s^{-1}. The initial modulus of elasticity at the three strain rates is about 30 GPa. The stiffness of the material decreases after the stiffness change point N. The $E_{changed}$ after the point N is only 28.9%, 31.2% and 29.4% of the initial elastic modulus $E_{initial}$, respectively.

The strength of tilt direction at quasi-static (10^{-3} s^{-1}), 10 s^{-1} and 100 s^{-1} strain rates are 158 MPa, 311 MPa and 331 MPa, respectively. The failure strains of the engineering are 0.115, 0.075 and 0.067. The strength increases with the increase of strain rate, while the engineering failure strain under two dynamic tension conditions is less than that under quasi-static tension (10^{-3} s^{-1}). The tilt direction is 45° with the weft direction, and the load is mainly borne by the matrix during tension. The stiffness change point N can also be found during the whole stretching process, and the strain after N point is greater than weft direction.

The strength of warp direction at quasi-static (10^{-3} s^{-1}), 10 s^{-1} and 100 s^{-1} strain rates are 383 MPa, 861 MPa and 997 MPa, respectively. The failure strains of the engineering are 0.045, 0.063 and 0.062. The change characteristics of strength and engineering failure strain are similar to that of weft direction. When the strain rate is 100 s^{-1}, the stiffness change point is obtained by calculating the second derivative of the curve. The stiffness change point N in warp direction is similar to that in weft direction.

Tensile strength, engineering failure strain and stiffness before and after N point at different strain rates and directions are shown in Tables 1, 2 and 3.

In practical application, the tensile load of GFRP is mainly shared by glass fibers, while the matrix resin plays a more fixed role. Due to the directionality of the internal glass fibers, GFRP exhibits anisotropy in tensile strength and

Table 1 Experimental and analytical results in different directions under quasi-static conditions

Direction	Tensile strength/MPa	Engineering failure strain	$E_{initial}$/GPa	$E_{changed}$/GPa	$E_{initial}/E_{changed}$ (%)
Weft	569	0.028	30.5	8.8	28.9
Tilt	158	0.115	6.8	0.7	10.3
Warp	383	0.045	9.9	2.7	27.3

Table 2 Experimental and analytical results in different directions under 10 s^{-1} strain rate

Direction	Tensile strength/MPa	Engineering failure strain	$E_{initial}$/GPa	$E_{changed}$/GPa	$E_{initial}/E_{changed}$ (%)
Weft	1209	0.058	33.3	10.4	31.2
Tilt	311	0.075	14.2	1.6	11.3
Warp	861	0.063	29.4	9.7	33.0

Table 3 Experimental and analytical results in different directions under 100 s^{-1} strain rate

Direction	Tensile strength/MPa	Engineering failure strain	$E_{initial}$/GPa	$E_{changed}$/GPa	$E_{initial}/E_{changed}$ (%)
Weft	1448	0.058	28.6	8.4	29.4
Tilt	331	0.067	18.8	1.6	8.5
Warp	997	0.062	23.4	11.3	48.3

other parameters. Weft direction and warp direction are the reinforcing directions of the fibers, and they all have obvious strain rate effects. The directions of weft and warp are the strengthening directions of GFRP, both of which have obvious strain rate effect. All three directions have a stiffness change point N, after which the stiffness of the material decreases. The values of $E_{changed}$ in weft and warp directions are about 30% to 50% of $E_{initial}$, while $E_{changed}$ in tilt direction is only about 10% of $E_{initial}$.

The three strain rates considered in the manuscript indicated that the mechanical properties of the composites were affected differently in different ranges of the strain rates. However, the glass fiber properties are insensitive to a strain rate in a range from 10^{-3} to 100 s^{-1}. The mechanical properties of GFRP materials are influenced by matrix resin and glass fiber, which also influenced by the restraint between resin matrix and glass fiber. Due to the interaction of the three factors, strain rate effect appears in GFRP materials.

3.4 Acquisition of dynamic failure strain

Using high-speed photography and DIC technology, dynamic failure parameters in different directions at 100 s^{-1} strain rate were obtained. The X and Y directions represent the tensile direction and the direction perpendicular to the tensile direction, respectively. Figures 16, 17 and 18 show the specimen morphology and strain field at the moment of fracture. The strain changes in the X and Y directions during dynamic tension are also shown.

It can be obtained from the graph that the final fracture data of the material under dynamic tension at 100 s^{-1} strain rate are $\varepsilon_x = 0.280$ and $\varepsilon_y = -0.088$. Considering that the specimen is a two-dimensional specimen, it can be assumed that ε_y is equal to ε_z in numerical value. Stress and strain are second-order tensors. When the spherical tensor is neglected and only the partial tensor is considered, the concepts of equivalent stress and strain can be introduced. The equivalent strain at the fracture is the dynamic failure strain.

$$\varepsilon_{eff} = \frac{\sqrt{2}}{3}\sqrt{(\varepsilon_x - \varepsilon_y)^2 + (\varepsilon_y - \varepsilon_z)^2 + (\varepsilon_z - \varepsilon_x)^2}$$

By substituting the corresponding values into the formulas above, we can get the following result $\varepsilon_{eff} = 0.245$.

The morphology, strain field distribution, strain curves in X and Y directions of specimens in tilt and warp directions are shown as follows.

Similarly, the dynamic failure strains in tilt direction and warp direction are 0.373 and 0.341 under dynamic tension at 100 s^{-1} strain rate. The dynamic failure strain in warp direction is close to that in tilt direction, and quite different from that in weft direction.

Finally, the dynamic tensile parameters of this GFRP material at strain rate of 100 s^{-1} are obtained as follows (Table 4).

Due to the uneven distribution of strain field in dynamic tensile process, the dynamic failure strain at material fracture is quite different from the conventional engineering
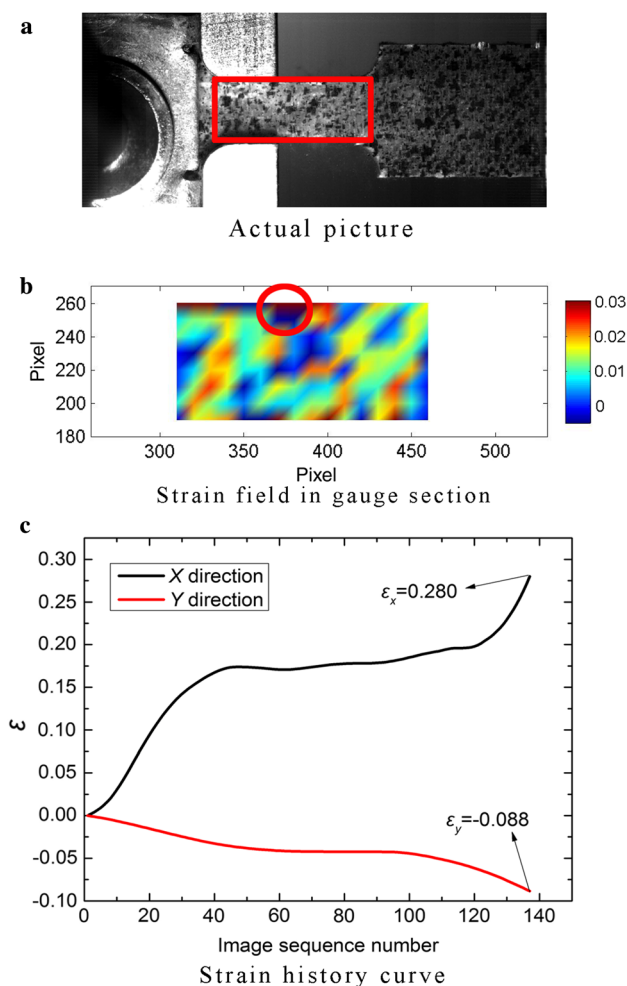
Fig. 16 Dynamic failure region in the weft direction under 100 s^{-1} strain rate

Fig. 17 Dynamic failure region in the tilt direction under 100 s^{-1} strain rate

failure strain. The engineering failure strain in weft, tilt and warp directions is only 23.7%, 18.0% and 18.2% of the dynamic failure strain, respectively. The dynamic failure strain of materials can be determined to understand the dynamic properties of materials more accurately, and the failure behavior of structures under dynamic loading can be better simulated in the analysis of actual structures.

4 Verification of parameters

Mat59 model in DYNA software is selected to simulate the impact three-point bending test. In the previous part, we obtained the parameters of GFRP composites. This part verifies the accuracy of these parameters. Using the comparison of numerical results and experimental results, the accuracy of parameters was determined.

The constitutive parameters of GFRP composites were obtained by experiment and parameter fitting. The
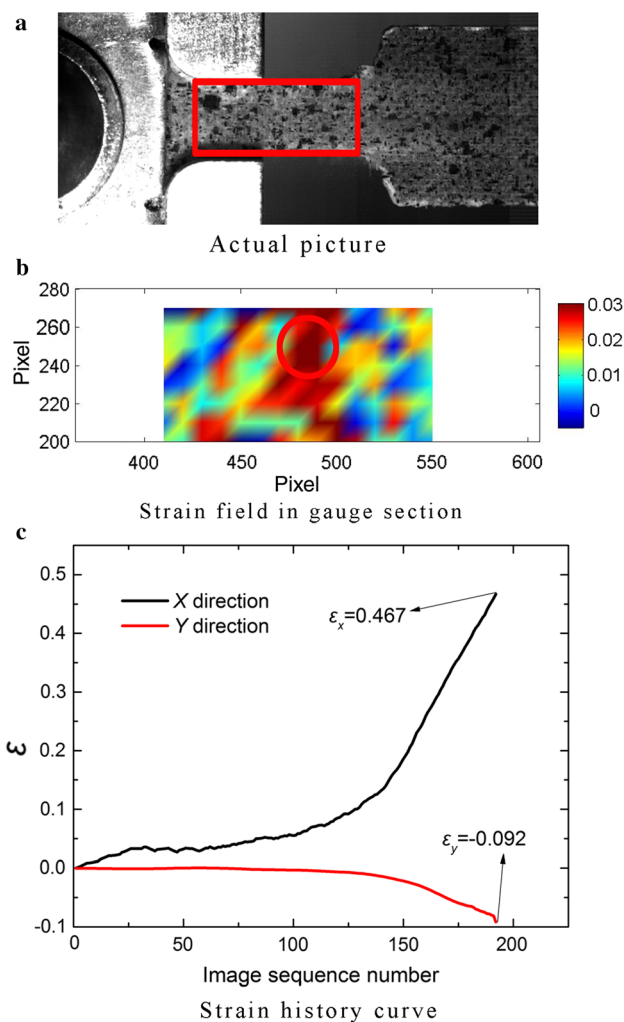
parameters obtained by DIC technology are substituted into the constitutive model of materials. The calculation model uses the same loading and boundary conditions as the real test case. After the calculation and experimental results are obtained, the two results are compared and analyzed. The accuracy of parameters of GFRP composites are verified by comparing the deformation morphology of impacted bi-directional reinforced glass fiber composites.

The consistency between the two methods can be used to verify the accuracy of constitutive parameters of bi-directional reinforced glass fiber composites. In the specific verification scheme, drop hammer test machine was used to carry out impact three-point bending test for bi-directional reinforced glass fiber composites, and 500 mm and 1000 mm drop heights were selected to carry out the experiment. The impact velocities at two impact heights are 3.1 m/s and 4.4 m/s, respectively. The whole impact three-point bending experimental device is shown as Fig. 19.
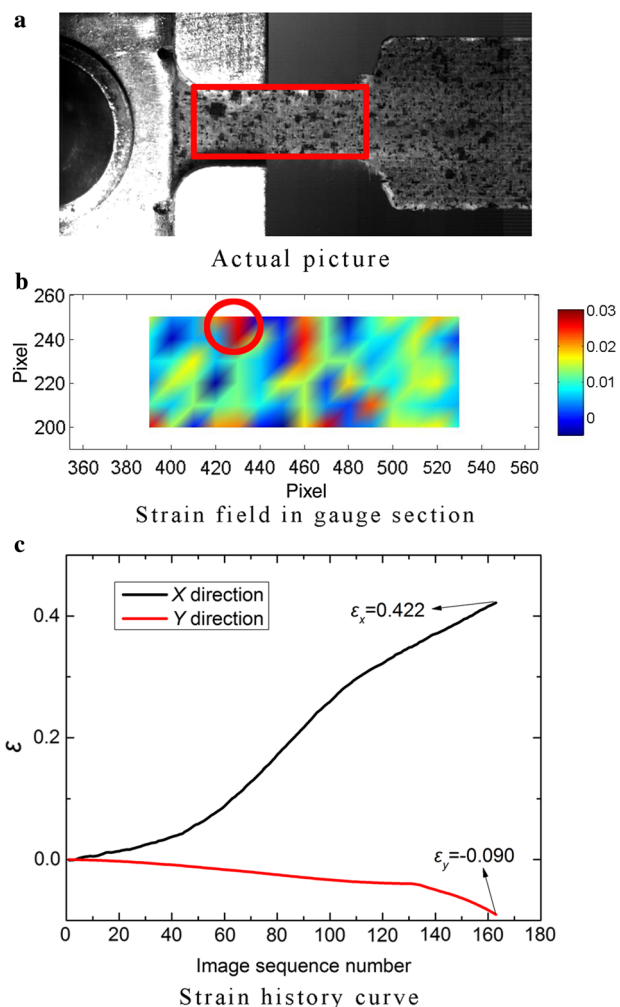
Fig. 18 Dynamic failure region in the warp direction under $100\ s^{-1}$ strain rate

Table 4 Dynamic failure strain and other relevant parameters in different directions

Direction	$E_{initial}$/GPa	σ_f/MPa	ε_f	ε_{eff}	$\varepsilon_f/\varepsilon_{eff}$ (%)
Weft	28.6	1448	0.058	0.245	23.7
Tilt	18.8	331	0.067	0.373	18.0
Warp	23.4	997	0.062	0.341	18.2

In order to obtain the real-time morphology of the impacted bi-directional reinforced glass fiber composites, high-speed camera was used to take pictures during the whole falling process. In order to facilitate high-speed photography to take clear pictures of lighter color bi-directional reinforced glass fiber composites under strong light during the shooting process, paint was specially sprayed on the side of the bi-directional reinforced glass fiber composites.

Fig. 19 Experimental device for impact three-point bending
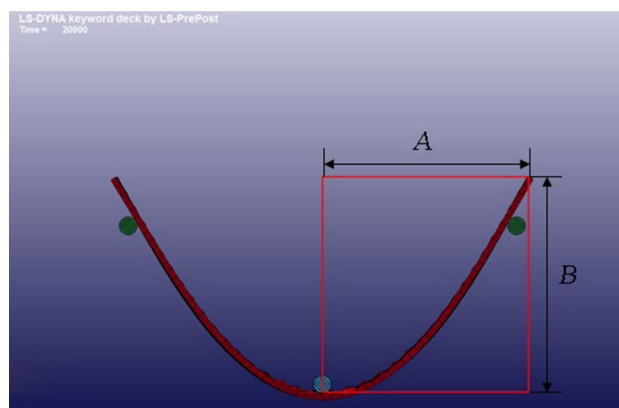

Fig. 20 Aspect ratio of rectangle

As shown in Fig. 20. At any moment in the process of numerical simulation, there exists a lowest point of hammer and a highest point of GFRP. A rectangle can be determined by combining the warp direction, the horizontal direction, the highest point and the lowest point mentioned above. The length of the rectangle in horizontal direction is A, and the length in warp direction is B. There is a aspect ratio ($r=A/B$) at any time of simulation, and there is a corresponding aspect ratio ($r^*=A^*/B^*$) in the actual impact test. Define deformation mode as the absolute value of $(r-r^*)/r$.

The height of the first verification condition is 500 mm. As shown in Fig. 21 five typical moments of the process are selected to compare the deformation morphology.

The difference of the deformation mode in the drop hammer impact experiment and the numerical simulation experiment are used to compared. The morphologies in 9.6 ms, 14.6 ms and 20.6 ms were compared. The aspect ratios under impact test and simulation test is calculated first, and then the percentage of the difference of aspect ratios in numerical simulation case is calculated. This percentage will be used as an index to measure the difference between the two.
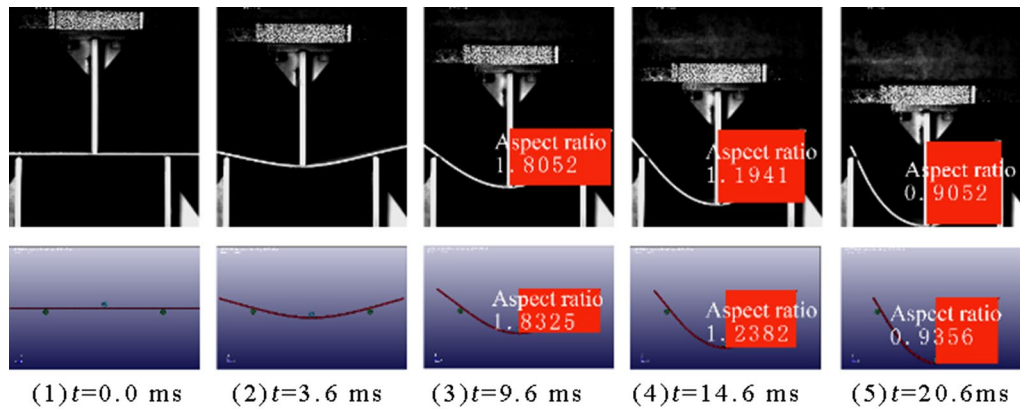
Fig. 21 Morphological comparison of 500 mm height drop

From Fig. 21, the difference of the aspect ratio of the two at 9.6 ms, 14.6 ms and 20.6 ms is 1.49%, 3.56% and 3.25%, respectively. The difference remained within 4% in all three moments.

The height of the second verification condition is 1000 mm. As shown in Fig. 22 five typical moments of the process are selected to compare the deformation morphology.

The difference in 4.8 ms, 7.3 ms and 10.2 ms is 2.11%, 1.28% and 2.10%, respectively. The difference remained within 3% in all three moments.

The deformation morphology of the bi-directional reinforced glass fiber composites under two working conditions is in good agreement with the numerical results. The difference of the three typical time deformation under the two working conditions is less than 4%, which proves the accuracy of the constitutive model.

5 Conclusion

In order to study the dynamic mechanical properties of GFRP composites, a series of static/dynamic tests were designed. The stress–strain curves of GFRP composites with different directions and strain rates were obtained by high-speed photography and DIC technology. The experimental results under different directions and strain rates are compared. The dynamic failure behavior of materials is accurately described by dynamic failure strains in different directions. At the same time, the experimental results are brought into the DYNA finite element software to simulate the impact three-point bending test, and the simulation results are compared with the experiment to verify the effectiveness of the method and parameters. The main conclusions are as follows:

1. Under different strain rates (10^{-3} s^{-1}, 10 s^{-1}, 100 s^{-1}), the material has the highest strength in weft direction and the highest engineering failure strain in tilt direction.
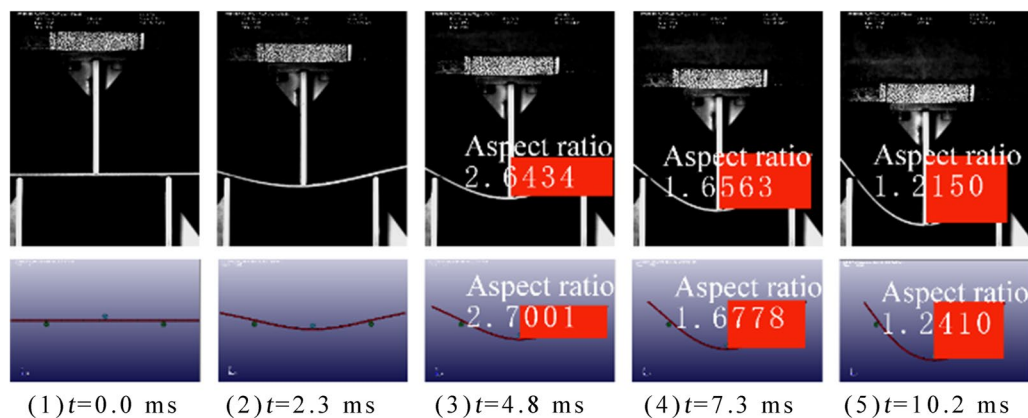

Fig. 22 Morphological comparison of 1000 mm height drop

The strength and engineering failure strain in the warp direction are moderate.

2. A stiffness change point N can be used to divide the tensile process into two stages. The change of stiffness can be divided into two stages. The values of $E_{changed}$ in weft and warp directions are about 30% to 50% of $E_{initial}$, while $E_{changed}$ in tilt direction is only about 10% of $E_{initial}$.

3. The engineering failure strain in weft, tilt and warp directions is only 23.7%, 18.0% and 18.2% of the dynamic failure strain, respectively.

4. The parameters are verified by the impact three-point bending test. The accuracy of the parameters is verified by comparing the deformation morphology. The experimental results provide a reference for the design of GFRP structures.

References

1. Tran, P., Nguyen, Q.T., Lau, K., et al.: Fire performance of polymer-based composites for maritime infrastructure. Comp. Part B Eng. **155**, 31–48 (2018)
2. Suzuki, T., Mahfuz, H., Takanashi, M., et al.: A new stiffness degradation model for fatigue life prediction of GFRPs under random loading. Int. J. Fatigue **119**, 220–228 (2019)
3. Morgado, T., Silvestre, N., Correia, J.R., et al.: Simulation of fire resistance behaviour of pultruded GFRP beams—Part II: stress analysis and failure criteria. Compos. Struct. **188**, 519–530 (2018)
4. Benmokrane, B., Nazair, C., Loranger, M., et al.: Field durability study of vinyl-ester-based GFRP rebars in concrete bridge barriers. J. Bridge Eng. **23**, 04018094 (2018)
5. Yao, K., Yang, Y., Li, H., et al.: Material characterization of a multi-cavity composite structure for the bogie frame of urban maglev train. Comp. Part B Eng. **99**, 277–287 (2016)
6. Blaznov, A.N., Krasnova, A.S., Krasnov, A.A., et al.: Geometric and mechanical characterization of ribbed FRP rebars. Polym. Testing **63**, 434–439 (2017)
7. Zhang, S., Caprani, C.C., Heidarpour, A., et al.: Influence of fibre orientation on pultruded GFRP material properties. Compos. Struct. **204**, 368–377 (2018)
8. Songlin, Z., Xi, L.: Lightweight design of vehicle components based on strengthening effects of low amplitude loads below fatigue limit. Fatigue Fract. Eng. Mater. Struct. **35**, 269–277 (2012)
9. Koo, J.S., Cho, H.J.: Theoretical method for predicting the weight reduction rate of a box-type car body for rolling stock by material substitution design. Int. J. Automot. Technol. **10**, 355–363 (2009)
10. Rochard, B.P., Schmid, F.: Benefits of lower-mass trains for high speed rail operations. Proc. Inst. Civil Eng. Transp. **157**, 51–64 (2004)
11. Cecchel, S., Ferrario, D., Panvini, A., et al.: Lightweight of a cross beam for commercial vehicles: development, testing and validation. Mater. Des. **149**, 122–134 (2018)
12. Onder, A., Robinson, M.: Harmonised method for impact resistance requirements of E-glass fibre/unsaturated polyester resin composite railway car bodies. Thin-walled Struct. **131**, 151–164 (2018)
13. Lee, S.J., Moon, D.Y., Ahn, C.H., et al.: A precast slab track partially reinforced with GFRP rebars. Comput. Concr. **21**, 239–248 (2018)
14. Tino, S.R., de Aquino, E.M.: Fracture characteristics and anisotropy in notched glass fiber reinforced plastics. Mater. Res. Ibero Am. J. Mater. **17**, 1610–1619 (2014)
15. Van, P.P., Mohareb, M.: A shear deformable theory for the analysis of steel beams reinforced with GFRP plates. Thin-walled Struct. **85**, 165–182 (2014)
16. Shang, J., Bai, Y., Xu, S., et al.: Dynamic constitutive equation of GFRP obtained by Lagrange experiment. Chin. Sci. Bull. **45**, 1164–1169 (2000)
17. Huang, Z., Nie, X., Xia, Y., et al.: Effect of strain rate and temperature on the dynamic tensile properties of GFRP. J. Mater. Sci. **39**, 3479–3482 (2004)
18. Asprone, D., Cadoni, E., Prota, A., et al.: Strain-rate sensitivity of a pultruded E-glass/polyester composite. J. Compos. Constr. **13**, 558–564 (2009)
19. Reis, P.N., Neto, M.A., Amaro, A.M., et al.: Effect of the extreme conditions on the tensile impact strength of GFRP composites. Compos. Struct. **188**, 48–54 (2018)
20. Chen, D.J., Chiang, F.P., Tan, Y., et al.: Digital speckle-displacement measurement using a complex spectrum method. Appl. Opt. **32**, 1839–1849 (1993)
21. Sjodahl, M., Benckert, L.: Electronic speckle photography: analysis of an algorithm giving the displacement with subpixel accuracy. Appl. Opt. **32**, 2278–2284 (1993)
22. Zhang, Z., Kang, Y., Wang, H., et al.: A novel coarse-fine search scheme for digital image correlation method. Measurement **39**, 710–718 (2006)
23. Pan, B.: Reliability-guided digital image correlation for image deformation measurement. Appl. Opt. **48**, 1535–1542 (2009)
24. Chang, S., Wang, C., Xiong, C., et al.: Nanoscale in-plane displacement evaluation by AFM scanning and digital image correlation processing. Nanotechnology **16**, 344–349 (2005)
25. Yoneyama, S., Kitagawa, A., Kitamura, K., et al.: In-plane displacement measurement using digital image correlation with Lens distortion correction. JSME Int. J. Series A-solid Mech. Mater. Eng. **49**, 458–467 (2006)
26. Kawahashi, M., Hirahara, H.: Velocity and density field measurements by digital speckle method. Opt. Laser Technol. **32**, 575–582 (2000)
27. Lu, H.M., Cary, P.D.: Deformation measurements by digital image correlation: implementation of a second-order displacement gradient. Exp. Mech. **40**, 393–400 (2000)
28. Bornert, M., Bremand, F., Doumalin, P., et al.: Assessment of digital image correlation measurement errors: methodology and results. Exp. Mech. **49**, 353–370 (2009)
29. Chen, J., Zhan, N., Zhang, X., et al.: Improved extended digital image correlation for crack tip deformation measurement. Opt. Lasers Eng. **65**, 103–109 (2015)
30. Rohde, S., Bennett, A.I., Harris, K.L., et al.: Measuring contact mechanics deformations using DIC through a transparent medium. Exp. Mech. **57**, 1445–1455 (2017)
31. Pan, B., Yu, L., Zhang, Q., et al.: Review of single-camera stereo-digital image correlation techniques for full-field 3D shape and deformation measurement. Sci. China Technol. Sci. **61**, 2–20 (2018)
32. Raghuwanshi, N.K., Parey, A.: Experimental measurement of spur gear mesh stiffness using digital image correlation technique. Measurement **111**, 93–104 (2017)
33. Malowany, K., Malesa, M., Kowaluk, T., et al.: Multi-camera digital image correlation method with distributed fields of view. Opt. Lasers Eng. **98**, 198–204 (2017)